Distribution of Tropospheric Water Vapor in Clear and Cloudy Conditions from Microwave Radiometric Profiling

ALIA IASSAMEN

Laboratoire d'Aérologie, Observatoire Midi-Pyrénées, Université Paul Sabatier, Toulouse, France, and LAMPA, Département d'Electronique, Université Mouloud Mammeri, Tizi Ouzou, Algeria

HENRI SAUVAGEOT

Laboratoire d'Aérologie, Observatoire Midi-Pyrénées, Université Paul Sabatier, Toulouse, France

NICOLAS JEANNIN

Département Electromagnétisme et Radar, Office National d'Etudes et de Recherches Aérospatiales, Toulouse, France

SOLTANE AMEUR

LAMPA, Département d'Electronique, Université Mouloud Mammeri, Tizi Ouzou, Algeria

(Manuscript received 19 November 2007, in final form 14 August 2008)

ABSTRACT

A dataset gathered over 369 days in various midlatitude sites with a 12-frequency microwave radiometric profiler is used to analyze the statistical distribution of tropospheric water vapor content (WVC) in clear and cloudy conditions. The WVC distribution inside intervals of temperature is analyzed. WVC is found to be well fitted by a Weibull distribution. The two Weibull parameters, the scale (λ) and shape (k), are temperature (T) dependent; k is almost constant, around 2.6, for clear conditions. For cloudy conditions, at $T <$ $-10°C$, k is close to 2.6. For $T > -10°C$, k displays a maximum in such a way that skewness, which is positive in most conditions, reverses to negative in a temperature region approximately centered around 0°C (i.e., at a level where the occurrence of cumulus clouds is high). Analytical $\lambda(T)$ and $k(T)$ relations are proposed. The WVC spatial distribution can thus be described as a function of T. The mean WVC vertical profiles for clear and cloudy conditions are well described by a function of temperature of the same form as the Clausius–Clapeyron equation. The WVCcloudy/WVCclear ratio is shown to be a linear function of temperature. The vertically integrated WV (IWV) is found to follow a Weibull distribution. The IWV Weibull distribution parameters retrieved from the microwave radiometric profiler agree very well with the ones calculated from the 15-yr ECMWF reanalysis (ERA-15) meteorological database. The radiometric retrievals compare fairly well to the corresponding values calculated from an operational radiosonde sounding dataset.

1. Introduction

Water vapor is a component of paramount importance in the atmosphere in relation to weather and climate sensitivity research. It is the main greenhouse gas and plays a predominant role in cloud dynamics through the release of wide amounts of latent heat with con-

densation. Water vapor content distribution (WVCD) is also very important in scientific fields related to the electromagnetic propagation in the microwave domain. Knowing the WVCD is thus essential for numerous environmental sciences (e.g., Peixoto et al. 1992; Chahine 1992; Webster 1994; Watson 2001; Soden and Held 2006; Sherwood et al. 2006). Points of particular interest concern the parameterization of WVCD and the quantitative differences of WVCD between clear and cloudy atmosphere. Climatological column water vapor content varies only slightly with the cloud cover in tropical regions but is significantly lower in clear sky

Corresponding author address: Dr. Henri Sauvageot, Laboratoire d'Aérologie, Université Paul Sabatier, Campistrous 65300 Lannemezan, France.
E-mail: sauh@aero.obs-mip.fr

than in cloudy sky at midlatitudes and the variation is not simply due to differences in atmospheric temperature distribution, as shown by Gaffen and Elliott (1993). The shape of WVCD has not been discussed and that of integrated water vapor (IWV) is, again, a point in discussion (e.g., Zhang et al. 2003; Foster et al. 2006).

Atmospheric water vapor is very difficult to quantify and describe because of the various physical and dynamical processes affecting its distribution, notably on short time and space scales. The in situ data used to analyze the tropospheric WVCD were mainly collected by radiosonde observations (Liu et al. 1991; Gaffen and Elliott 1993; Foster et al. 2006; Miloshevich et al. 2006). However, radiosonde observations do not permit one to associate tightly the presence of clouds and the WVC profiles. Some fragmentary, in space and time, in situ observations were also gathered from aircraft (Spichtinger et al. 2004; Korolev and Isaac 2006). In clear air and in the daytime, the total column water vapor from the surface was measured with a simple near-infrared sun photometer (Brooks et al. 2007). Water vapor in upper atmospheric layers was observed by remote sensing from the Geostationary Operational Meteorological Satellite using the 6.7-μm channel (e.g., Soden and Bretherton 1993) and from infrared sounders such as the Atmospheric Infrared Sounder (AIRS). Observations were also made using microwave sensors such as the Upper Atmospheric Research Satellite (UARS) microwave limb sounder (Stone et al. 2000) or from Advanced Microwave Sounding Unit (AMSU) instruments and Special Sensor Microwave Imager (SSM/I) instruments or by combining the two kinds of data (Kidder and Jones 2007). Vertically integrated (column) water vapor, or precipitable water, data were obtained from global positioning system (GPS) signals (e.g., Rocken et al. 1997; Liou et al. 2001; Van Baelen et al. 2005; Foster et al. 2006). Standard dual-channel ground-based microwave radiometers, with a frequency close to the 22.235-GHz water vapor line and the other in a window at higher frequency, were used to measure IWV and liquid water path (LWP) simultaneously (e.g., Hogg et al. 1983; Snider 2000; Westwater et al. 2004; van Meijgaard and Crewell 2005).

The tropospheric vertical profile of water vapor mixing ratio was also observed by active remote sensing, notably by Raman lidar by Sakai et al. (2007) in the nighttime from a ground-based device, and by Whiteman et al. (2007) in the daytime with an airborne spectroscopic lidar. Upper-troposphere water vapor was measured by differential absorption lidar technique (Ferrare et al. 2004). However, lidar measurements work only in the absence of optically thick clouds. Information on humidity profiles has been obtained with wind profiling radars from the refractive index gradient inferred from the echo power using variational assimilation (Furumoto et al. 2007) and by combining wind profiler and ground-based radiometer data (Bianco et al. 2005) or with GPS data (Furumoto et al. 2003). The above quoted techniques are not able to provide the data required to analyze the WVC distribution on short time and space scales, in clear and cloudy conditions.

More recently, a ground-based multichannel microwave radiometric technique was proposed for the retrieval of temperature, water vapor, and liquid water profiles (Solheim et al. 1998; Solheim and Godwin 1998; Güldner and Spänkuch 2001; Ware et al. 2003). This new technique has not yet gained the confidence of long-used methods and its accuracy is not that of in situ measurements, but it offers some opportunities to capture the differences between clear and cloudy vertical profiles, which are still poorly known and documented because of a lack of relevant data.

The object of the present paper is to discuss the form of the WVCDs and to propose their parameterization as a function of the temperature to quantify the differences between clear and cloudy sky conditions. The paper is based on a set of data collected with a multichannel microwave radiometric profiler.

2. Data

a. Water vapor parameters

The quantity retrieved by the radiometer (cf. section 2b) is the water vapor density of the moist air, or absolute humidity, ρ. Water vapor approximately behaves as an ideal gas, with each mole of gas obeying an equation of state that can be written

$$\rho_w = \frac{e_w}{R_w T}, \qquad (1)$$

where e_w is the partial pressure of the water vapor (hPa), R_w is the gas constant for water vapor (i.e., $R_w = R/m_w$, where R is the universal gas constant and m_w is the mass of one mole of vapor), and T is the absolute temperature (K). Usually ρ_w is multiplied by 10^6 and expressed in grams per meter cubed.

At saturation, (1) is

$$\rho_{s,w} = \frac{e_{s,w}}{R_w T_s}, \qquad (2)$$

where the subscript s refers to saturation. The temperature variation of the pressure at which the phase transition takes place is given by the Clausius–Clapeyron equation, which can be written for equilibrium over water and over ice. A large number of equations were proposed to calculate the saturation pressure over

a surface of liquid water or ice. Murphy and Koop (2005) review the vapor pressure of ice and supercooled water for atmospheric applications. They conclude that all of the commonly used expressions for the vapor pressure of water and ice are very close to each other for tropospheric temperature. In the present work, a formulation derived from the Magnus equation, convenient for routine computation, is used [cf. Pruppacher and Klett 1997, p. 117, Eqs. (4-83) and (4-84) and Appendix A-4-8]. No enhancement factor (defined as the ratio of the saturation vapor pressure of moist air to that of pure water vapor; e.g., Buck 1981) is used. This factor is very small and depends on air pressure. It gives for water

$$e_{s,w}(T) = e_{s,w}(T_0) \, \exp\left[\frac{A_w(T - T_0)}{T - B_w}\right], \qquad (3)$$

with $e_{s,w}$ in hectopascals, T in kelvins, $e_{s,w}(T_0) = 6.1070$ hPa, $T_0 = 273.15$ K, $A_w = 17.15$, and $B_w = 38.25$ K, and for ice

$$e_{s,i}(T) = e_{s,i}(T_0) \, \exp\left[\frac{A_i(T - T_0)}{T - B_i}\right], \qquad (4)$$

with $e_{s,i}$ in hectopascals, T in kelvins, $e_{s,i}(T_0) = 6.1064$ hPa, $T_0 = 273.15$ K, $A_i = 21.88$, and $B_i = 7.65$ K. At the triple point, for $T_s = T_0$, we have $e_{s,w} = e_{s,i} = 611.154$ Pa, with $e_s/R_w = 1.32 \times 10^3$ and $R_w = 0.463$ J K^{-1} g^{-1}.

Using (3) and (4) in (2) gives the vapor density at saturation over water and ice respectively, namely with the numeric coefficients

$$\rho_{s,w} = \frac{1.32 \times 10^3}{T_s} \exp\left[\frac{17.15\,(T_s - 273.15)}{T_s - 38.25}\right] \qquad (5)$$

and

$$\rho_{s,i} = \frac{1.32 \times 10^3}{T_s} \exp\left[\frac{21.88\,(T_s - 273.15)}{T_s - 7.65}\right], \qquad (6)$$

with ρ in grams per meter cubed and temperature in kelvins.

b. Microwave radiometric measurements

The data were collected with a microwave radiometric profiler TP/WVP-3000 manufactured by Radiometrics. This radiometer is described in several papers (e.g., Solheim and Godwin 1998; Ware et al. 2003; Liljegren et al. 2004) and online (www.radiometrics.com). In short, this instrument measures 12 radiometric brightness temperatures through a sequential scan of 12 frequencies inside the microwave spectrum, 5 in the K band between 22.035 and 30.000 GHz, on the flank of the 22-GHz water

vapor absorption line, and 7 in the V band between 51.250 and 58.800 GHz, on the flank of the 60-GHz molecular oxygen complex. The bandwidth for each channel is 300 MHz. The beamwidth is 5°–6° at 22–30 GHz and 2°–3° at 51–59 GHz.

The radiometer also includes some in situ sensors for the ground-level measurement of temperature, pressure, and humidity, as well as a zenith-looking infrared radiometer with a 5° beamwidth and a liquid water (precipitation) detector. The combination of the cloud-base temperature provided by the IR sensor with the retrieved temperature profile gives an estimate of the cloud-base height. The cloud-base height can be associated with warm liquid or ice (e.g., cirrus), or with mixed clouds. The combination of temperature and WVC enables the calculation of the relative humidity at each level.

The 22–30-GHz channels are calibrated to 0.3-K RMS by automated tipping procedures. The 51–59-GHz channels are calibrated to 0.5-K RMS with a liquid nitrogen target (Han and Westwater 2000; Westwater et al. 2001). Liquid nitrogen calibration is performed regularly (about each month) and when the radiometer is moved.

The time cycle of the whole 12-channel scanning process is about 23 s. However, for the present study, the time interval between profiles is only 92 s, which means that only one profile out of four was retained to reduce statistical redundancy.

Inputs include the 12 microwave brightness temperature measurements, one infrared temperature, as well as temperature, humidity, and pressure at surface level, representing 16 inputs. By inversion of the radiances measured at the different channels through a neural network application, the radiometer retrieves, up to a height of 10 km, the vertical profiles of temperature and water vapor, cloud-base temperature and height, vertically integrated water vapor, and liquid water (ILW). The neural network profile retrieval is based on a training from historical series of local radiosondes (Schroeder and Westwater 1991; Solheim et al. 1998; Liljegren et al. 2004). Brightness temperatures in the 5-K-band channels are calculated with the revised absorption model proposed by Liljegren et al. (2004).

c. Accuracy and resolution

The profiler retrieval accuracy was discussed and estimated from a comparison with simultaneous radiosonde data (Güldner and Spänkuch 2001; Liljegren et al. 2001, 2004; Ware et al. 2003). Such comparisons are approximate because of spatial and volume sampling differences between radiosonde and radiometer measurements. The neural network method is found to be slightly less accurate than a statistical regression method

TABLE 1. Dataset.

Subset location and designation	Obs periods	Duration (day)	Profiles rejected (%)	No. of clear sky profiles	No. of cloudy sky profiles
Aire-sur-l'Adour	13–15 Mar 2007 29–31 Mar 2007 1–15 Apr 2007	21	4.81	6166 (32.85%)	12 603 (67.15)
Toulouse 1	1–18 Dec 2006 1–20 Jan 2007	38	9.31	6650 (20.55%)	25 710 (79.45%)
Toulouse 2	21–31 Jan 2008 1–29 Feb 2008 1–31 Mar 2008 1–6 Apr 2008	77	9.72	23 754 (36.39%)	41 521 (63.61%)
Lannemezan 1	26–31 Jan 2007 1–27 Feb 2007	32	7.35	13 970 (50.18%)	13 869 (49.82%)
Lannemezan 2	24–30 Apr 2007 1–29 May 2007 5–28 Jun 2007	60	11.78	8131 (16.36%)	41 572 (83.64%)
Lannemezan 3	2–31 Jul 2007 1–31 Aug 2007 1–30 Sep 2007 1–31 Oct 2007 1–19 Nov 2007	141	12.40	31 384 (27.06%)	84 597 (72.94%)
Total		369	10.55	90 055 (29.39%)	219 872 (70.61%)

[see Güldner and Spänkuch (2001) for the resulting vertical profiles of accuracy]. The information content of the measurements degrades with altitude. The vertical resolution in retrieved temperature linearly changes from about 0.1 km near the surface to ~6 km at a height of 8 km. For vapor density, the resolution falls from 0.3 km near the surface to 1.5 km at a height of 6 km and 3.5 km at 10 km (Güldner and Spänkuch 2001; Liljegren et al. 2004).

Accuracy is degraded when there is liquid water on the radome of the radiometer and in the presence of heavy precipitation above the radiometer, like with other microwave radiometers. Retrievals are not applicable in this case. Light precipitation aloft with a dry radome is acceptable. A field campaign was performed in March and April 2007 at Aire-sur-Adour (Table 1; Fig. 1) to compare the TP/WVP-3000 radiometric profiler with radiosoundings. The analysis of the results is out of the scope of the present paper and will be discussed elsewhere. However, it can be briefly stated that, for accuracy and resolution, the results for the TP/WVP-3000 radiometer are in agreement with the conclusions of the previous studies quoted above.

Figure 1 shows, as an example, the temporal series of ILW, IWV, binary detection of rain presence at the surface, cloud-base height as estimated by the IR temperature combined with temperature profile, and air temperature measured at surface level for 9 days, from 8 to 16 April 2004 at Toulouse (cf. section 2d for location). The air temperature displays the usual diurnal varia-

tions with a trend toward warming from day 4 to day 8. For day 9, the diurnal oscillation is very small because the air temperature is dominated by a wide rainy system sweeping the site during the last 14 h of the series.

In the presence of rain reaching the surface in Fig. 1, the microwave radiometer does not to work correctly. ILW, notably, displays peaks that always exceed 2 mm (this threshold is never reached in the absence of rain), and the cloud-base height is seen near or at the surface. The IWV is less sensitive to the presence of rain. This justifies the removal of the profiles with ILW > 2 mm (cf. section 2d). In clear sky, the IR thermometer reads −49.8°C, an arbitrary rounded down value meaning that there is no cloud above. The height of the corresponding level can be seen to increase from day 4 to day 9. ILW and IWV are strongly correlated but neither of them is correlated with surface air temperature. In other words, there is no significant diurnal variation of ILW and IWV, which are dominated by the general circulation of the synoptic-scale structures.

To assess how the results presented in the present paper are biased by the retrieval uncertainty, we need to know the RMS error vector affecting the retrieved profiles. Because we do not know this vector, we have used the RMS error vectors computed from a similar 12-channel microwave radiometer operated by the Atmospheric Radiation Measurement (ARM) Program in Germany between March and December 2007, namely the error vector for "Black Forest Germany" available online (http://www.archive.arm.gov). We believe that
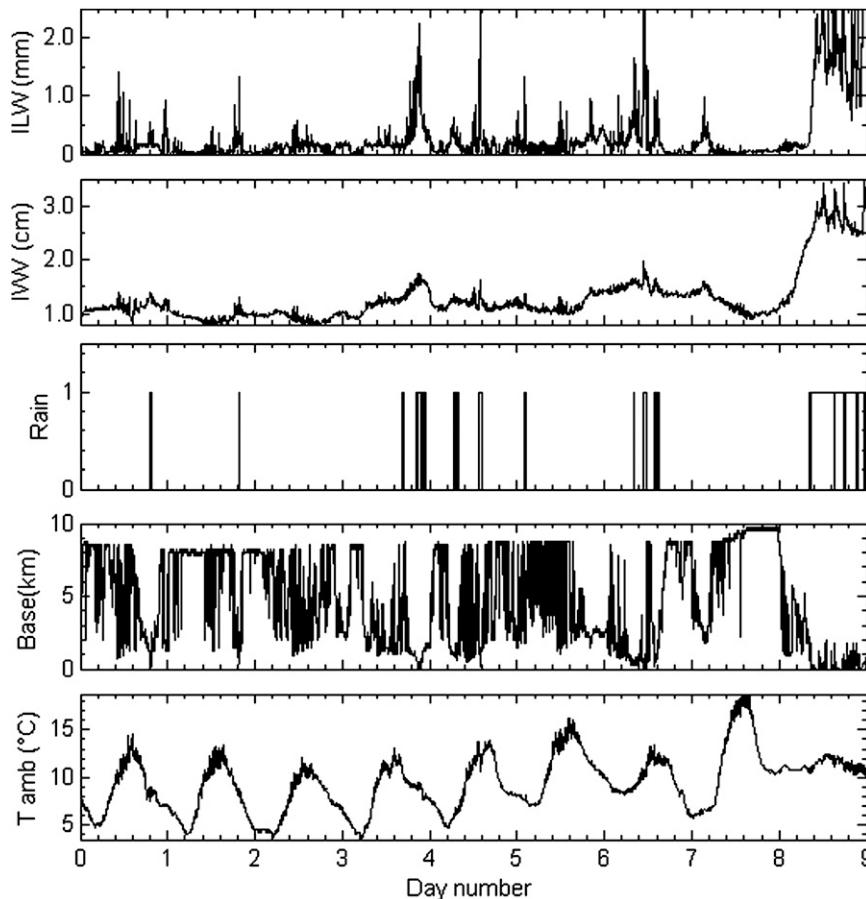
FIG. 1. Radiometer-observed time series of (top to bottom) ILW, IWV, rain detection (binary), cloud-base height, and surface air temperature for 9 days, from 8 to 16 Apr 2004.

this error vector is representative of our west European climatic area and convenient for the uses in the present paper. To compute the RMS error on the retrievals, we have added to each retrieved profile a Gaussian noise with zero mean and a standard deviation equal to the RMS error for each layer.

d. Site and dataset

The data were collected at three different sites located in the southwest of France during six periods distributed over the four seasons as specified in Fig. 2 and Table 1. This dataset is considered to be representative of coastal oceanic midlatitude climate (e.g., Martyn 1992; see also arguments in section 4). During the data acquisition at the various sites, it rained for 7.5% of the time (the long-term mean in this area is 8%), clouds were present 72% of the time, and clear sky 28% of the time.

Profile retrievals are obtained at 250-m intervals from the surface to 10 km, which represents 41 levels (or range

bins) including the surface level where temperature, humidity, and pressure are measured by in situ sensors.

The training of the neural network was performed with 10 yr of radiosonde data (2 per day) from Bordeaux-Mérignac, a meteorological station located on the Atlantic coast (Fig. 2). Upper-air data at Bordeaux-Mérignac are assumed to be representative of the atmosphere over coastal, oceanic, midlatitude western Europe.

One profile, corresponding to one 23-s measurement cycle, was retained every 92 s, which gives 309 927 profiles for all 369 days of the observing period. One profile includes, in fact, the three 41-level basic profiles of temperature, WVC, and RH, the two integrated values IWV and ILW, and the surface parameters. Profiles associated with the presence of rain as detected by the rain detector of the radiometer were removed, as well as the profiles associated with an ILW higher than 2 mm. ILW > 2 mm is due to the presence of precipitation aloft that can bias the retrievals (Snider 2000). The remaining profiles (89.45%) were classified in two subsets
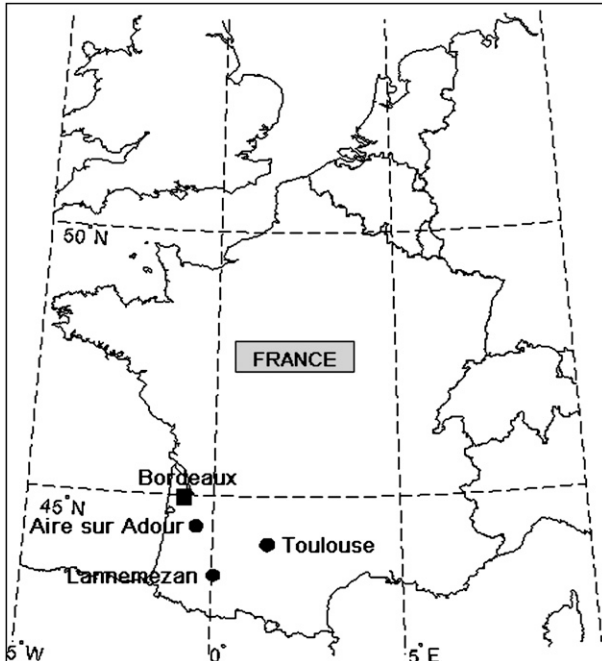
FIG. 2. Map showing the location of the data collection sites and radiosonde station (Bordeaux).
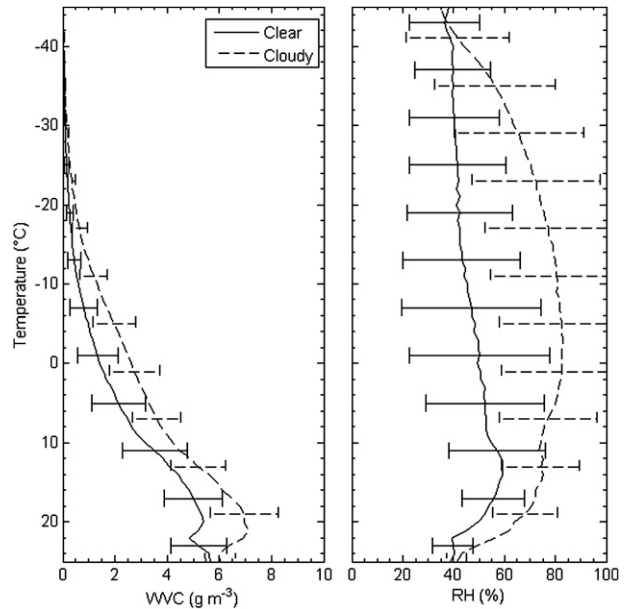

FIG. 3. Mean vertical profiles of (left) WVC and (right) RH retrieved from the microwave radiometric profiler for clear and cloudy conditions for the subset Toulouse 2 (21 Jan–31 Mar 2008).

considering the cloud-base temperature (t_{base} in degrees Celsius) data from the IR radiometer:

1) clear sky profiles when $t_{base} \leq -49.8°C$—90 055 profiles were included in this subset, and
2) cloudy sky profiles, when $t_{base} > -49.8°C$, made up of 219 872 profiles.

When a profile was removed, for example for not satisfying the ILW condition, all of the other data of the profile were rejected.

Differences between beamwidth of the IR radiometer and microwave channels may cause a classification in clear category for profiles with microwave beam partly filled with cloud. This case is encountered in the presence of a nonuniform cloud cover, notably with cumulus clouds, when clouds go into or out of the beam while they are advected over the radiometer. We looked for profiles with $t_{base} \leq -49.8°C$ and ILW higher than the minimum detectable value of the radiometer and found that <1% of profiles were meet this criteria. These were classified as cloudy.

Mean vertical profiles of WVC and relative humidity as a function of temperature, for clear and cloudy conditions, over the subset Toulouse 2 (winter), are presented in Fig. 3 with the standard deviation bars. For the vertical coordinate, temperature was preferred to altitude because water vapor content depends only on temperature. Using altitude as the vertical coordinate blurs the

representation of vertical profiles of WV parameters. The upper limit of the profiles has been taken at $-45°C$ because at colder temperatures, WVC can fall below the minimum detectable, which is about 0.02 g m^{-3}. The mean vertical profile of temperature versus altitude averaged over the dataset (almost one year) is not presented because it is not of interest. In fact, it shows a quasilinear decrease of T from $10°C$ at the surface to $-55°C$ at 10-km altitude, that is, the standard atmospheric lapse rate of $-6.5°C$ km^{-1}. At a given altitude, temperature for cloudy conditions is slightly warmer (about $0.5°C$) than that for clear conditions.

Figure 3 shows that the clear and cloudy profiles for WVC present a monotonic decreases from 6–7 g m^{-3} near the surface to <0.1 g m^{-3} at temperatures <$-40°C$, with some irregularities for temperatures >20°C. These irregularities (inversion of the vertical gradient) are thought to be associated with the convective boundary layer structure. Profiles of RH increase from the surface up to about $0°C$, then decrease above. This variation with

TABLE 2. Definition of the parameters used in the present paper.

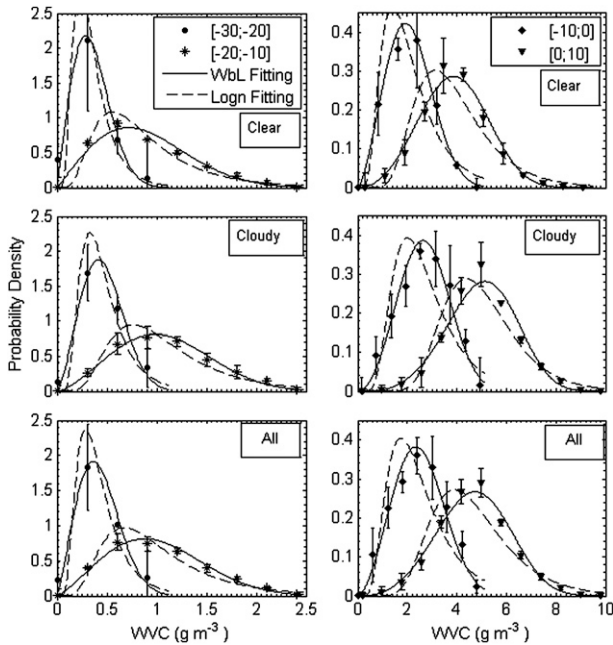| Distribution	Variable	Parameter	
	x	Mean μ_x	Variance σ_x^2
Lognormal (logn)	$y = \ln x$	Mean μ_y	Variance σ_y^2
Weibull (wbl)	x	Scale λ	Shape k

FIG. 4. Pdfs of WVC for four temperature classes between 10° and −30°C—(left) −30 to −20 and −20 to−10; (right) −10 to 0 and 0 to 10— and Weibull best fitting for the three datasets: (top) clear sky, (middle) cloudy sky, and (bottom) all. The corresponding numerical values are given in Table 3. The error bars were computed with the ARM error vectors. Note that coordinate scales are different for the left and right panels.

T can be seen as resulting from the combination of the effect of cloud liquid water vertical distribution, which displays a maximum at midtropospheric levels (e.g., Mazin 1995; Gultepe and Isaac 1997), and the monotonic decrease of WVC with temperature.

3. Water vapor content distribution

To analyze the WVC distribution, three datasets are considered—clear sky, cloudy sky, and all (i.e., the sum of clear and cloudy sky subsets)—to emphasize the differences between clear and cloudy. Probability density functions (pdfs) were calculated using temperature classes of width $\Delta T = 10°C$ and WVC bins of 0.2 g m^{-3}, between 20° and −45°C. The data were fitted using two analytical forms: lognormal and Weibull. These forms were selected among others from empirical tests and from physical and bibliographical considerations. They are frequently used for atmospheric and cloud characteristic representation because they are related to physical processes relevant for atmospheric phenomena. The lognormal distribution is associated with the statistical process of proportionate effects (see Aitchison and Brown 1966, p. 22; Crow and Shimizu 1988): the change in the variate at any step of the process is a random proportion of the previous value of the variate. The lognormal form is found to be convenient for many cloud characteristics such as rain cell size distributions (Mesnard and Sauvageot 2003), rain-rate distributions (Atlas et al. 1990; Sauvageot 1994), precipitable water (Foster et al. 2006), and relative humidity (Soden and Bretherton 1993; Yang and Pierrehumbert 1994). The Weibull form is found to be convenient for variables whose distribution is limited by extreme values, for example, life variables or wind when the velocity is limited by turbulence. For the WVC distribution, the upper limit is the vapor density at saturation ρ_s in the presence of condensation (cloudy case). In clear air there is no upper limit.

The lognormal probability density function is written

TABLE 3. Fitting parameters for the water vapor content pdf (Fig. 4): μ_y and σ_y are the mean and standard deviation of the lognormal distribution, λ and k are the scale and shape of the Weibull distribution, respectively, and r is the correlation coefficient. WVC unit is grams per meter cubed.

| Temperature class (°C) | Clear | | | | | | Cloudy | | | | | | All | | | | | |
| | Lognormal | | | Weibull | | | Lognormal | | | Weibull | | | Lognormal | | | Weibull | | |
	μ_y	σ_y	r	λ	k	r	μ_y	σ_y	r	λ	k	r	μ_y	σ_y	r	λ	k	r
−45 to −35	−2.50	0.51	1.00	0.10	2.19	1.00	−2.38	0.57	1.00	0.12	2.07	1.00	−2.42	0.55	1.00	0.12	2.08	1.00
−40 to −30	−2.05	0.49	0.99	0.16	2.18	0.81	−1.83	0.51	0.93	0.20	2.25	0.96	−1.91	0.51	0.87	0.19	2.17	0.93
−35 to −25	−1.62	0.49	0.98	0.25	2.11	0.99	−1.34	0.48	0.99	0.30	2.34	0.98	−1.43	0.50	0.99	0.30	2.20	0.99
−30 to −20	−1.18	0.52	0.99	0.40	2.04	0.97	−0.88	0.48	0.99	0.52	2.39	0.98	−0.98	0.51	0.99	0.48	2.20	0.98
−25 to −15	−0.73	0.54	0.99	0.63	2.01	0.98	−0.40	0.49	0.97	0.80	2.41	0.98	−0.55	0.52	0.97	0.74	2.21	0.98
−20 to −10	−0.27	0.56	0.98	1.00	2.02	0.97	−0.03	0.49	0.96	1.22	2.45	0.99	−0.12	0.53	0.96	1.14	2.25	0.98
−15 to −5	0.20	0.56	0.95	1.59	2.15	0.98	0.42	0.49	0.94	1.91	2.55	0.99	0.34	0.52	0.94	1.79	2.35	0.99
−10 to 0	0.62	0.52	0.88	2.37	2.48	0.98	0.90	0.45	0.82	3.02	2.99	0.97	0.81	0.50	0.85	2.80	2.68	0.98
−5 to 5	0.99	0.46	0.89	3.29	2.92	0.99	1.28	0.36	0.85	4.19	3.85	0.99	1.19	0.42	0.85	3.93	3.34	0.99
0 to 10	1.29	0.39	0.94	4.35	3.23	0.99	1.57	0.30	0.96	5.51	4.09	0.98	1.49	0.35	0.94	5.19	3.61	0.99
5 to 15	1.51	0.33	0.98	5.27	3.59	0.98	1.81	0.28	0.99	6.99	3.86	0.96	1.73	0.32	0.98	6.58	3.51	0.97
10 to 20	1.67	0.32	0.97	6.14	3.71	0.97	1.98	0.29	0.99	8.34	3.89	0.98	1.93	0.32	0.98	7.98	3.59	0.98
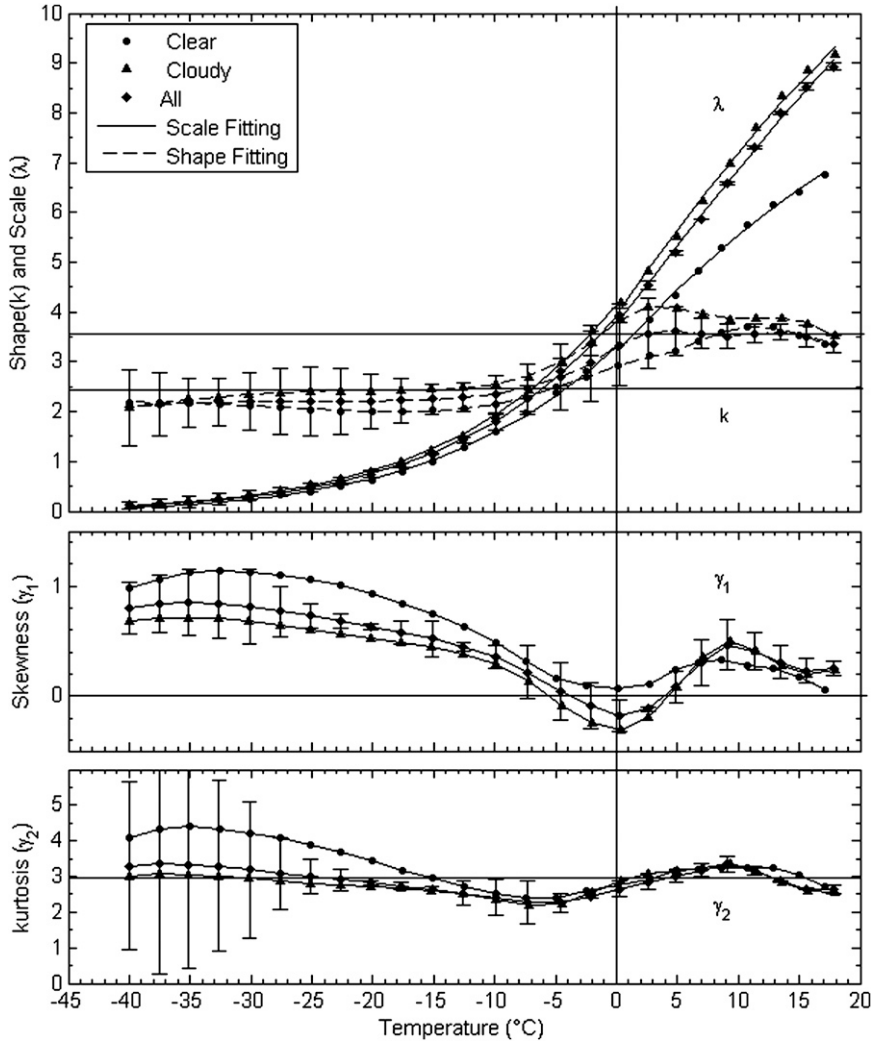
FIG. 5. Variation as a function of the temperature of the two parameters of the Weibull distribution, (top) shape k and scale λ, and of (middle) skewness and (bottom) kurtosis for the pdf of WVC calculated for 24 classes of temperature of width $\Delta T = 5°C$ between $-45°$ and $20°C$. The error bars were computed with the ARM error vectors. For the sake of clarity, only the error bars for the curves all are drawn. (top) Horizontal lines at $k = 2.6$ and 3.6 show the domain where pdfs are quasi normal.

$$f(x\,;\mu_y,\sigma_y) = \frac{1}{\sqrt{2\pi}x\sigma_y}\exp\left[-\frac{1}{2}\left(\frac{y-\mu_y}{\sigma_y}\right)^2\right], \quad (7)$$

where $y = \ln x$ (Table 2). The two parameters of the distribution are the mean μ_y and variance σ_y^2 of y, defined as

$$\mu_y = \ln\left\{\mu_x\left[1 + \left(\frac{\sigma_x}{\mu_x}\right)^2\right]^{1/2}\right\} \quad (8)$$

and

$$\sigma_y^2 = \ln\left[1 + \left(\frac{\sigma_x}{\mu_x}\right)^2\right]. \quad (9)$$

The Weibull pdf is

$$f(x\,;k,\,\lambda) = \frac{k}{\lambda}\left(\frac{x}{\lambda}\right)^{k-1}\exp\left[-\left(\frac{x}{\lambda}\right)^k\right]. \quad (10)$$

The two parameters of the distribution are the scale λ and the shape k. The mean μ_x and variance σ_x^2 are defined as

$$\mu_x = \lambda\Gamma(1 + 1/k) \quad (11)$$

TABLE 4. Fitting parameters for the shape curve of Fig. 5 [Eq. (13)]; r is the correlation coefficient.

	a_1	b_1	c_1	a_2	b_2	c_2	r
$T > 0°C$							
Clear	3.70	285	17.3	0.543	273	2.74	0.99
Cloudy	3.11	274	8.21	3.68	288	11.7	0.99
All	1.91	273	7.58	3.51	288	15.1	0.97
$T \leq 0°C$							
Clear	2.02	282	15.1	2.22	227	74.1	0.99
Cloudy	4.71	287	13.6	2.42	252	50.2	0.99
All	1.59	279	9.6	2.23	256	100	0.99

TABLE 5. Fitting parameters for the scale curve of Fig. 5 [Eq. (14)]; r is the correlation coefficient.

	a_3	b_3	c_3	r
$T > 0°C$				
Clear	884	1.81	252	0.99
Cloudy	1103	2.14	249	0.99
All	1039	2.43	245	0.99
$T \leq 0°C$				
Clear	913	10.8	124	0.99
Cloudy	1147	16.8	54.9	0.99
All	1079	17.2	51.9	0.99

and

$$\sigma_x^2 = \lambda^2 \Gamma(1 + 2/k) - \mu^2, \qquad (12)$$

where Γ is the gamma function.

Figure 4 shows the probability density of WVC, data points, best-fitting curves, and error bars for 4 classes of temperature out of 12 (for the sake of clarity). The numeric values of the fitting parameters and correlation coefficients are given in Table 3. For the clear case, lognormal and Weibull distributions are almost equivalent. Lognormal is slightly better for $T < -15°C$ and Weibull is slightly better for $T > -15°C$. For the cloudy case, Weibull is better than lognormal at temperatures between $-20°$ and $10°C$ and the two distributions are almost equivalent at $T < -20°C$ and $> 10°C$. It is the
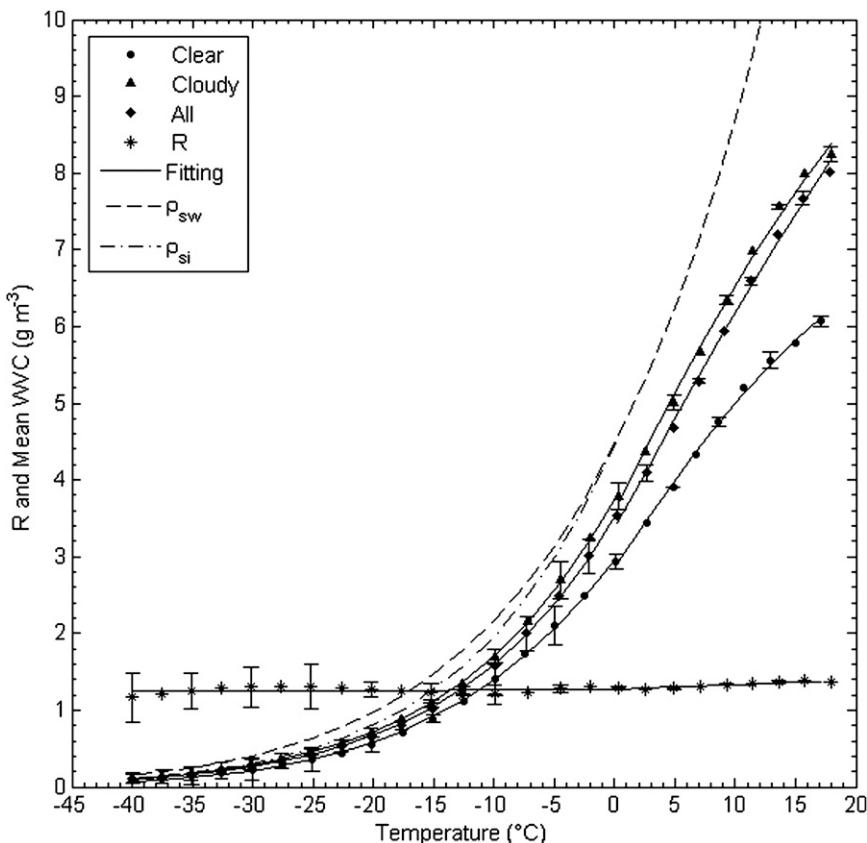

FIG. 6. Variation as a function of the temperature of the mean WVC, of the ratio R = WVCcloudy/WVCclear and best-fitted curves. Curves $\rho_{s,w}$ and $\rho_{s,i}$ give the water vapor density at saturation with respect to liquid water and ice, respectively. The error bars were computed with the ARM error vectors.

TABLE 6. Fitting parameters of the mean WVC for the curves of Fig. 6 [Eq. (15)]; r is the correlation coefficient.

	A	B	C	r
$T > 0°C$				
Clear	787	1.76	253	0.99
Cloudy	998	2.05	250	0.99
All	933	2.35	246	0.99
$T \leq 0°C$				
Clear	814	11.5	117	0.99
Cloudy	1035	20.1	18.9	0.99
All	968	19.6	26.3	0.99

same for all, which is dominated by the cloudy case. The Weibull fitting gives better results because the WVC fluctuations have limits related to the condensation process when the WVC reaches saturation.

The various coefficients of Table 3 are not very sensitive to the width of the temperature classes ΔT. Similar results are obtained for ΔT up to 15°, but beyond it degrades. On the other hand, the coefficients display large differences for clear and cloudy cases.

Figure 5 (top panel) shows the variation as a function of temperature of the WVC pdf Weibull parameters calculated for 24 temperature classes of width $\Delta T = 5°C$, between −45° and 20°C. Figure 5 (lower panels) displays the corresponding Fisher's coefficients of skewness (γ_1) and kurtosis (γ_2). For $\gamma_1 > 0$, skewness is on the left side (the mode is lower than the average) and there is a tail on the right side. For $\gamma_1 < 0$, it is the reverse, that is to say skewness is on the right and tail on the left. Partly, γ_1 and k convey the same kind of information. For $k < 2.6$, the Weibull pdfs are positively skewed (with a right-side tail). For $2.6 < k < 3.6$, the skewness coefficient approaches zero (no tail), that is to say pdf is quasi normal. For $k > 3.6$, Weibull pdfs are negatively skewed, and the tail is on the left. This is what Fig. 5 shows. At cold temperature, WVC pdfs are positively skewed, more for clear than for cloudy. While temperature increases, skewness diminishes and WVC pdf evolves toward a normal shape. For temperature between about −2° and 12°C, k for cloudy pdfs is higher than 3.6, that is to say slightly negatively skewed. The clear case is positively skewed everywhere. For $T > 10°C$, clear and cloudy cases evolve toward the same value since the corresponding atmospheric level is clear for the two cases (i.e., below cloud base). Kurtosis variations are small around the normal value. The clear case is leptokurtic at cold temperature. Platykurtic character increases with temperature up to about −5°C, then at warmer temperature, a peak of leptokurtic character correlated with skewness is observed.
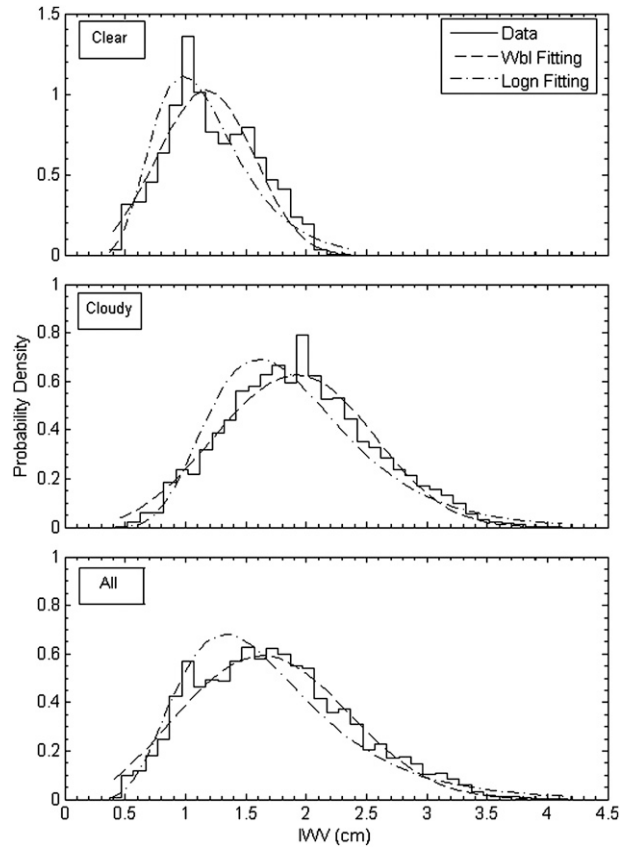

FIG. 7. Pdfs of vertically integrated water vapor for the three datasets and lognormal and Weibull best fitting. The numerical values are given in Table 7.

This evolution of the WVC Weibull pdf parameters with temperature can be explained, at least in part, by considering the WVC limit of saturation with respect to water and ice. In the absence of limit, WVC is lognormally distributed as most dynamically controlled atmospheric parameters are (cf. Crow and Shimizu 1988). Clear profiles are found in this case. Limits linked to saturation create a truncation on the right side of the pdfs and thus induce a reverse skewness. The bump observed on the k curve, for $-10° < T < 15°C$, corresponds tightly to the average liquid cloud water vertical distribution associated with midlatitude cumulus clouds (e.g., Mazin 1995; Gultepe and Isaac 1997).

TABLE 7. Fitting parameters for the IWV curve of Fig. 7; r is the correlation coefficient.

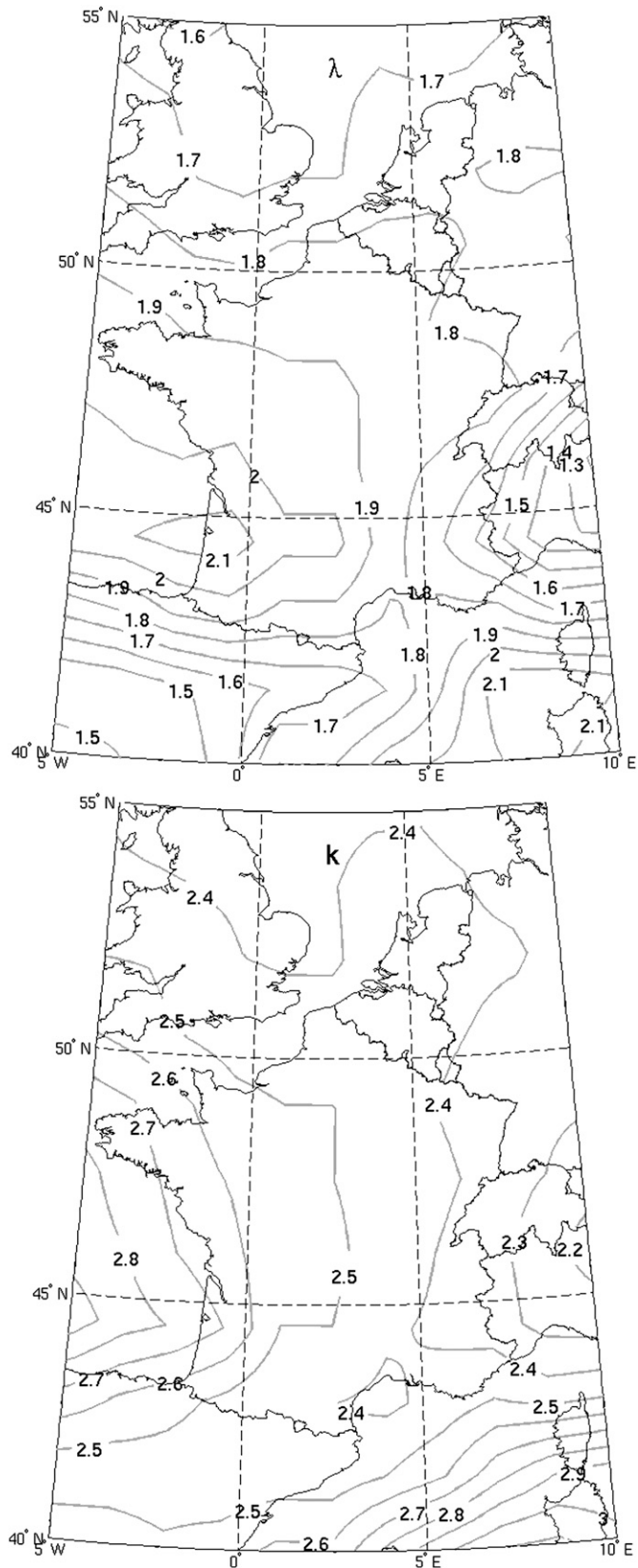|	Lognormal			Weibull		
	μ	σ	r	λ	k	r
Clear	0.10	0.34	0.93	1.30	3.45	0.92
Cloudy	0.59	0.34	0.97	2.12	3.44	0.98
All	0.45	0.41	0.96	1.90	2.86	0.98

FIG. 8. Isolines of the Weibull distribution parameters of IWV calculated from ERA-15: (top) λ and (bottom) k.

TABLE 8. As in Table 3 but calculated from the radiosonde dataset for the all case.

| Temperature class (°C) | All | | | | | |
| | Lognormal | | | Weibull | | |
	μ_y	σ_y	r	λ	k	r
−45 to −35	−2.43	0.52	1.00	0.11	2.33	1.00
−40 to −30	−2.10	0.61	1.00	0.16	1.91	1.00
−35 to −25	−1.59	0.61	0.90	0.27	1.96	0.98
−30 to −20	−1.13	0.63	0.94	0.43	1.93	0.99
−25 to −15	−0.67	0.62	0.91	0.68	2.01	0.98
−20 to −10	−0.25	0.62	0.91	1.03	2.00	0.97
−15 to −5	0.17	0.63	0.89	1.60	1.98	0.95
−10 to 0	0.60	0.63	0.80	2.45	2.06	0.91
−5 to 5	1.01	0.60	0.66	3.60	2.30	0.88
0 to 10	1.38	0.56	0.66	5.08	2.52	0.91
5 to 15	1.60	0.50	0.68	6.66	2.83	0.94
10 to 20	1.90	0.44	0.77	8.13	3.24	0.97

Curves $k(T)$ of Fig. 5 can be fitted with a general model of Gauss2 form, namely

$$k(T) = a_1 \exp\left[-\left(\frac{T - b_1}{c_1}\right)^2\right] + a_2 \exp\left[-\left(\frac{T - b_2}{c_2}\right)^2\right], \quad (13)$$

with coefficients given in Table 4.

Curves $\lambda(T)$ of Fig. 5 can be fitted very well with a general model similar to (5), that is,

$$\lambda(T) = \frac{a_3}{T} \exp\left[\frac{b_3 (T - 273.15)}{T - c_3}\right], \quad (14)$$

with coefficients given in Table 5 and T in kelvins.

Because it is more representative physically, the WVC mean, μ_{WVC}, has also been plotted and fitted as shown in Fig. 6. The coefficients of the fitting with a function of the form (5), namely

$$\mu_{WVC}(T) = \frac{A}{T} \exp\left[\frac{B (T - 273.15)}{T - C}\right], \quad (15)$$

are given in Table 6. Of course these coefficients are not far from those of Table 5. In Fig. 6, the saturation curves $\rho_{s,w}$ and $\rho_{s,i}$ given by (5) and (6) are also drawn.

Curves of Figs. 5 and 6 can be fitted acceptably with a single function for all the temperature ranges considered in the present work (from −40° to +20°C). However, similar to the saturation water vapor density Eqs. [(5) and (6)], a fitting slightly better is obtained when considering separately the parts <0° and >0°C. That is why Tables 4, 5, and 6 present these two parts.

To summarize, the mean of WVC in clear and cloudy conditions depends only on the temperature and is described accurately by (15) with the coefficients of Table 6.

From (15), using the coefficients of Table 6, the ratio of the mean of WVC for cloudy and clear conditions can be written

$$R = \frac{\mu_{WVC\,cloudy}}{\mu_{WVC\,clear}} = 0.0061T + 1.27 \quad \text{for} \quad T > 0\,°\text{C}$$
$$= 0.0007T + 1.27 \quad \text{for} \quad T \leq 0\,°\text{C}, \quad (16)$$

with T in degrees Celsius.

Using (13) and (14) in (10) enables the writing of the WVC pdf as a function of the sole temperature.

4. Distribution of IWV

As for WVC, the pdf of vertically integrated WVC (IWV) was calculated and fitted with lognormal and Weibull distributions for clear, cloudy, and all datasets. Curves are shown in Fig. 7. Fitting coefficients and correlation coefficients are given in Table 7. For clear conditions, the lognormal distribution gives a correlation coefficient slightly better than the Weibull one, but for cloudy and for all, the Weibull distribution is the best. Using a wide radiosonde and GPS dataset, Foster et al. (2006) found that the precipitable water (i.e., IWV) distribution can be well fitted with a lognormal distribution. They emphasize that, for tropical oceanic environments, IWV tends to exhibit negatively skewed histograms for which fitting with a reverse lognormal distribution is proposed.

Using the 15-yr European Centre for Medium-Range Weather Forecasts (ECMWF) reanalysis (ERA-15) meteorological database, the Weibull parameters k and λ for the IWV distribution were calculated. Isolines of k and λ over the western European area, where the radiometric data were collected (as shown in Fig. 2), are
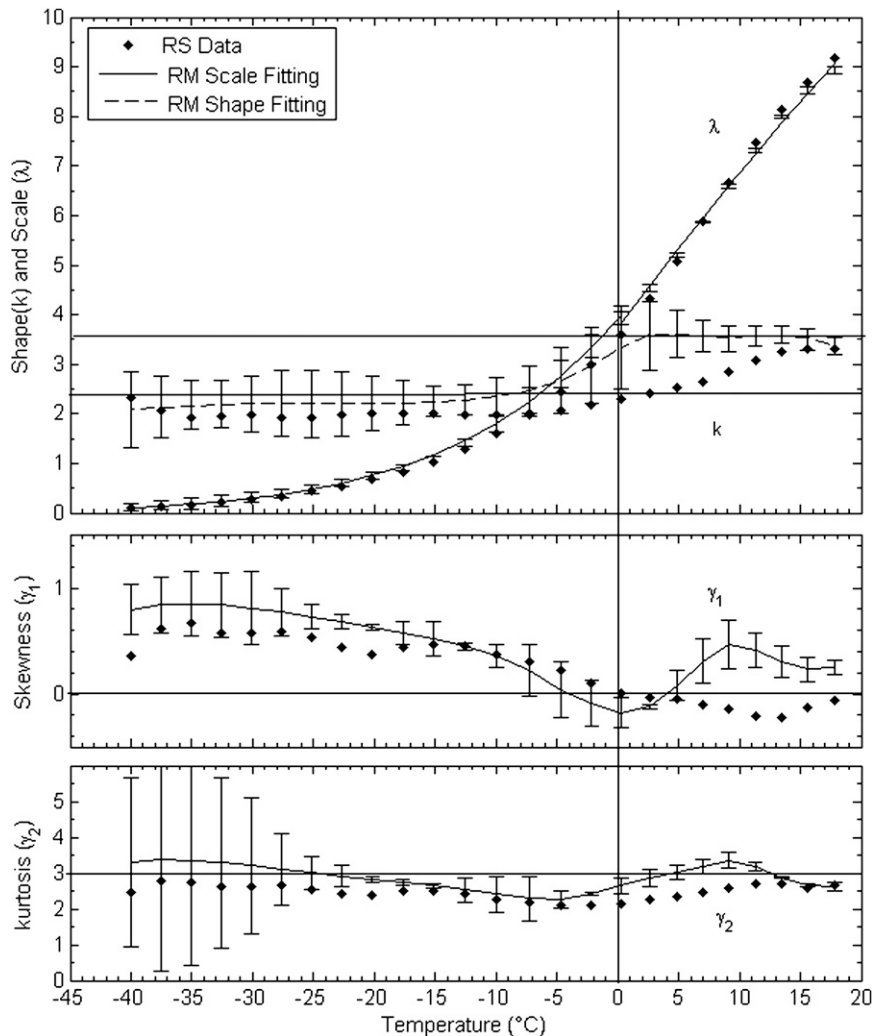
FIG. 9. The dots show the variation as a function of the temperature of the two parameters of the Weibull distribution, (top) shape k and scale λ, and (middle) the skewness and (bottom) kurtosis for the pdf of WVC calculated from the RS dataset for 24 classes of temperature of width $\Delta T = 5°C$ between $-45°$ and $20°C$. The curves and error bars are the radiometer retrievals for the all case redrawn from Fig. 5 for comparison with the RS values.

presented in Fig. 8. The fields of k and λ values are rather homogeneous, showing the validity of our assumption in section 2d that this area can be considered a single climatological entity for WVC distribution. Averaged values over the area represented in Fig. 8 are $k = 2.5$ and $\lambda = 1.9$, which compare very well with the values for all of Table 7, that is, $k = 2.8$ and $\lambda = 1.9$. This agreement can be seen as supporting the validity of the IWV radiometric measurements. In a companion paper analyzing the worldwide IWV distribution from the ERA-15 database (Jeannin et al. 2008), we found that k for tropical environment is negatively skewed, which agrees with Foster et al. (2006). For latitude lower than about 10°, k is higher than 6 with a peak at 10 in some

very humid equatorial areas (e.g., Amazonia and Indonesia).

5. Comparison with operational radiosonde soundings

Operational radiosonde soundings (RSs) provide data on the vertical WVC distribution along slanted trajectories 2 times a day, at 0000 and 1200 UTC. It is not possible to distinguish clear and cloudy vertical RS profiles in the same way that we do with the radiometric profiles. Besides, the RS sampling frequency does not permit one to capture some important aspects of the WVC distribution related to the WVC diurnal cycle.

However, a rough comparison can be made between the radiometer-retrieved WVC pdfs and profiles for the all case and those provided by a radiosonde dataset. To perform this comparison, we have used the two daily RSs gathered at Bordeaux during the period of 2006–08 when the radiometer was active (Table 1). The RS data considered for the statistic are taken over the altitude domain cover by the radiometer. For example, for the period when the radiometer was operated from Lannemezan (altitude 600 m), the RS data from Bordeaux (altitude 50 m) are taken above 600 m.

Table 8 gives the coefficients of the WVC pdfs calculated from the RS data and fitted with lognormal and Weibull functions. The Weibull fitting is clearly very good and better than the lognormal one. Coefficients λ and k of the RS pdfs versus temperature are represented in Fig. 9. In Fig. 9, we have redrawn the curves of Fig. 5 for the all case with their error bars and added the values calculated from the RS data. Scale λ from RS is very close to the radiometer retrieval one. Shape k from RS is, as in the radiometric one, almost constant and close to the radiometric values for $T < 5°C$. For $T > 5°C$ it is lower than the radiometric values but enclosed between 2.6 and 3.6—that is, quasi normal. Skewness and kurtosis also are very similar for RS and radiometer.

Figure 10 shows the WVC mean versus temperature. In Fig. 10 the curve of Fig. 6 for all with the error bars has been redrawn and the values calculated from RS have been superimposed. A detailed discussion of the differences between the radiometric retrievals and the RS values is out of the scope of the present paper. That is why by way of conclusion we limit ourselves to noting that the agreement for the pdf shape and the mean WVC variation with temperature is rather good.

6. Summary and conclusions

The distribution of the vapor phase of tropospheric water was studied from 369 days of observations collected in various sites of western Europe with a 12-frequency microwave radiometric profiler. Data were regrouped in two subsets, clear sky and cloudy sky. The profiles associated with the presence of rain were rejected.

Several forms of distribution were considered to fit the pdf of the atmospheric water vapor profiles observed with the profiler. For the sake of clarity, only lognormal and Weibull distributions were discussed in the present paper because they proved to be the most efficient for the pdf fitting. The lognormal function is associated with the statistical process of proportionate effect, frequently identified in the atmosphere. The Weibull function is convenient for random variables
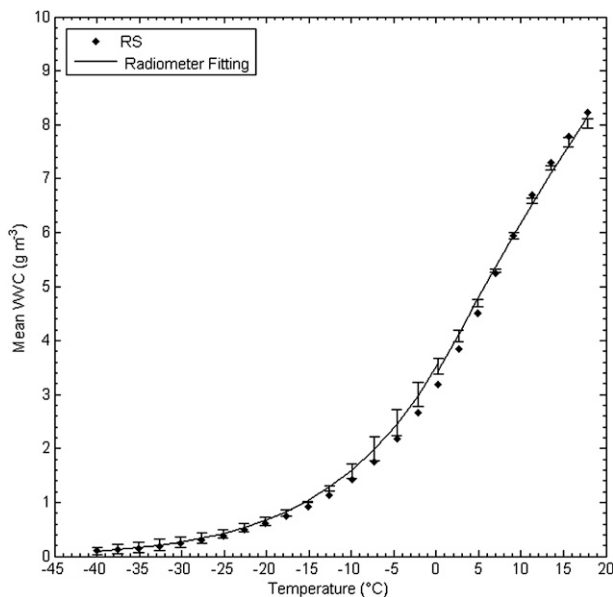

FIG. 10. The dots show the variation as a function of the temperature of the mean WVC calculated from the RS dataset for 24 classes of temperature of width $\Delta T = 5°C$ between $-45°$ and $20°C$. The curves and error bars are the radiometer retrievals for the all case redrawn from Fig. 6.

whose distributions are limited by extreme values such as water vapor with condensation.

The WVC pdf inside 10°C temperature classes between 20° and $-45°C$ is found to be accurately fitted by Weibull distributions. The two parameters of the Weibull distribution, the shape k and scale λ, are shown to be well described by analytical functions of temperature T. Using $k(T)$ and $\lambda(T)$ in the pdf enables the writing of the WVC spatial distribution as a function of T. The mean WVC vertical profile can be represented by a function of the temperature of the same form as the Clausius–Clapeyron equation. The ratio of mean WVC for cloudy to mean WVC for clear conditions is linearly dependent on T, with a mean value of 1.27.

The pdf of the vertically integrated WVC, or precipitable water, is found to be Weibull distributed rather than lognormal. The values retrieved from the microwave radiometric profiler compare very well with the ones calculated from the ERA-15 meteorological database.

A rough comparison between the radiometric retrievals and the values provided by an operational radiosonde sounding dataset shows that the agreement for the pdf shape and the mean WVC profile as a function of temperature is fairly good.

REFERENCES

Aitchison, J., and J. A. Brown, 1966: *The Lognormal Distribution.* Cambridge University Press, 176 pp.

Atlas, D., D. Rosenfeld, and D. A. Short, 1990: The estimation of convective rainfall by area integrals: 1. The theoretical and empirical basis. *J. Geophys. Res.,* **95** (D3), 2153–2160.

Bianco, L., D. Cimini, F. S. Marzano, and R. Ware, 2005: Combining microwave radiometer and wind profiler radar measurements for high-resolution atmospheric humidity profiling. *J. Atmos. Oceanic Technol.,* **22,** 949–965.

Brooks, D. R., F. M. Mims III, and R. Roettger, 2007: Inexpensive near-IR sun photometer for measuring total column water vapor. *J. Atmos. Oceanic Technol.,* **24,** 1268–1276.

Buck, A. L., 1981: New equations for computing vapor pressure and enhancement factor. *J. Appl. Meteor.,* **20,** 1527–1532.

Chahine, M. T., 1992: The hydrological cycle and its influence on climate. *Nature,* **359,** 373–380.

Crow, E. L., and K. Shimizu, 1988: *Lognormal Distributions.* CRC Press, 387 pp.

Ferrare, R. A., and Coauthors, 2004: Characterization of upper-troposphere water vapor measurements during AFWEX using LASE. *J. Atmos. Oceanic Technol.,* **21,** 1790–1808.

Foster, J., M. Bevis, and W. Raymond, 2006: Precipitable water and the lognormal distribution. *J. Geophys. Res.,* **111,** D15102, doi:10.1029/2005JD006731.

Furumoto, J.-I., K. Kurimoto, and T. Tsuda, 2003: Continuous observations of humidity profiles with the MU radar–RASS combined with GPS or radiosonde measurements. *J. Atmos. Oceanic Technol.,* **20,** 23–41.

——, S. Imura, T. Tsuda, H. Seko, T. Tsuyuki, and K. Saito, 2007: The variational assimilation method for the retrieval of humidity profiles with the wind-profiling radar. *J. Atmos. Oceanic Technol.,* **24,** 1525–1545.

Gaffen, D. J., and W. P. Elliott, 1993: Column water vapor content in clear and cloudy skies. *J. Climate,* **6,** 2278–2287.

Güldner, J., and D. Spänkuch, 2001: Remote sensing of the thermodynamic state of the atmospheric boundary layer by ground-based microwave radiometry. *J. Atmos. Oceanic Technol.,* **18,** 925–933.

Gultepe, I., and G. A. Isaac, 1997: Liquid water content and temperature relationship from aircraft observations and its applicability to GCMs. *J. Climate,* **10,** 446–452.

Han, Y., and E. Westwater, 2000: Analysis and improvement of tipping calibration for ground-based microwave radiometers. *IEEE Trans. Geosci. Remote Sens.,* **38,** 1260–1276.

Hogg, D. C., F. O. Guiraud, J. B. Snider, M. T. Decker, and E. R. Westwater, 1983: A steerable dual-channel microwave radiometer for measurement of water vapor and liquid in the troposphere. *J. Climate Appl. Meteor.,* **22,** 789–806.

Jeannin, N., L. Féral, H. Sauvageot, and L. Castanet, 2008: Statistical distribution of integrated liquid water and water vapor content from meteorological reanalysis. *IEEE Trans. Antennas Propag.,* **56,** 3350–3355.

Kidder, S. Q., and A. S. Jones, 2007: A blended satellite total precipitable water product for operational forecasting. *J. Atmos. Oceanic Technol.,* **24,** 74–81.

Korolev, A., and G. A. Isaac, 2006: Relative humidity in liquid, mixed-phase, and ice clouds. *J. Atmos. Sci.,* **63,** 2865–2880.

Liljegren, J. C., B. M. Lesht, S. Kato, and E. E. Clothiaux, 2001: Initial evaluation of profiles of temperature, water vapor and cloud liquid water from a new microwave profiling radiometer. Preprints, *11th Symp. on Meteorological Observations and Instrumentation,* Albuquerque, NM, Amer. Meteor. Soc., 8.6.

——, S. A. Boukabara, K. Cady-Pereira, and S. A. Clough, 2004: The effect of the half-width of the 22-GHz water vapor line on retrievals of temperature and water vapor profiles with a twelve-channel microwave radiometer. *IEEE Trans. Geosci. Remote Sens.,* **10,** 1–7.

Liou, Y. A., Y. T. Teng, T. Van Hove, and J. C. Liljegren, 2001: Comparison of precipitable water observations in the near tropics by GPS, microwave radiometer, and radiosondes. *J. Appl. Meteor.,* **40,** 5–15.

Liu, W. T., W. Tang, and P. P. Nüler, 1991: Humidity profiles over the ocean. *J. Climate,* **4,** 1023–1034.

Martyn, D., 1992: *Climates of the World.* Developments in Atmospheric Sciences, Vol. 18, Elsevier, 435 pp.

Mazin, I. P., 1995: Cloud water content in continental clouds of middle latitudes. *Atmos. Res.,* **35,** 283–297.

Mesnard, F., and H. Sauvageot, 2003: Structural characteristics of rain fields. *J. Geophys. Res.,* **108,** 4385, doi:10.1029/2002JD002808.

Miloshevich, L. M., H. Vömel, D. N. Whiteman, B. M. Lesht, F. J. Schmidlin, and F. Russo, 2006: Absolute accuracy of water vapor measurements from six operational radiosonde types launched during AWEX-G, and implications for AIRS validation. *J. Geophys. Res.,* **111,** D09S10, doi:10.1029/2005JD006083.

Murphy, D. M., and T. Koop, 2005: Review of the vapour pressures of ice and supercooled water for atmospheric applications. *Quart. J. Roy. Meteor. Soc.,* **131,** 1539–1565.

Peixoto, J. P., A. H. Oort, and E. N. Lorenz, 1992: *Physics of Climate.* American Institute of Physics, 520 pp.

Pruppacher, H. R., and J. D. Klett, 1997: *Microphysics of Clouds and Precipitation.* Kluwer Academic, 954 pp.

Rocken, C., T. Van Hore, and R. Ware, 1997: Near real-time GPS sensing of atmospheric water vapor. *Geophys. Res. Lett.,* **24,** 3221–3224.

Sakai, T., T. Nagai, M. Nakazato, T. Matsumura, N. Orikasa, and Y. Shoji, 2007: Comparison of Raman lidar measurements of tropospheric water vapor profiles with radiosondes, hygrometers on the meteorological observation tower, and GPS at Tsukuba, Japan. *J. Atmos. Oceanic Technol.,* **24,** 1407–1423.

Sauvageot, H., 1994: The probability density function of rain rate and the estimation of rainfall by area integrals. *J. Appl. Meteor.,* **33,** 1255–1262.

Schroeder, J. A., and E. R. Westwater, 1991: User's guide to WPL microwave radiative transfer software. NOAA Tech. Memo. ERL WPL-213, 37 pp.

Sherwood, S. C., E. R. Kursinski, and W. G. Read, 2006: A distribution law for free-tropospheric relative humidity. *J. Climate,* **19,** 6267–6277.

Snider, J. B., 2000: Long-term observations of cloud liquid, water vapor, and cloud-base temperature in the North Atlantic Ocean. *J. Atmos. Oceanic Technol.,* **17,** 928–939.

Soden, B. J., and F. P. Bretherton, 1993: Upper tropospheric relative humidity from the GOES 6.7 μm channel: Method and climatology for July 1987. *J. Geophys. Res.,* **98** (D9), 16 669–16 688.

——, and I. M. Held, 2006: An assessment of climate feedbacks in coupled ocean–atmosphere models. *J. Climate,* **19,** 3354–3360.

Solheim, F., and J. Godwin, 1998: Passive ground-based remote sensing of atmospheric temperature, water vapor, and cloud liquid profiles by a frequency synthesized microwave radiometer. *Meteor. Z.,* **7,** 370–376.

——, ——, E. Westwater, Y. Han, S. Keihm, K. Marsh, and R. Ware, 1998: Radiometric profiling of temperature, water vapor, and liquid water using various inversion methods. *Radio Sci.,* **33,** 393–404.

Spichtinger, P., K. Gierens, H. G. J. Smit, J. Ovarlez, and J. F. Gayet, 2004: On the distribution of relative humidity in cirrus clouds. *Atmos. Chem. Phys.,* **4,** 639–647.

Stone, E. M., L. Pan, B. J. Sandor, W. G. Read, and J. W. Waters, 2000: Spatial distributions of upper tropospheric water vapor measurements from UARS microwave limb sounder. *J. Geophys. Res.,* **105,** 12 149–12 161.

Van Baelen, J., J. P. Aubagnac, and A. Dabas, 2005: Comparison of near-real time estimates of integrated water vapor derived with GPS, radiosondes, and microwave radiometer. *J. Atmos. Oceanic Technol.,* **22,** 201–210.

van Meijgaard, E., and S. Crewell, 2005: Comparison of model predicted liquid water path with ground-based measurements during CLIWA-NET. *Atmos. Res.,* **75,** 201–226.

Ware, R., R. Carpenter, J. Güldner, J. Liljegren, T. Nehrkorn, F. Solheim, and F. Vandenberghe, 2003: A multichannel radiometric profiler of temperature, humidity and cloud liquid. *Radio Sci.,* **38,** 8079, doi:10.1029/2002RS002856.

Watson, R. T., and Coauthors, 2001: *Climate Change 2001: Synthesis Report.* Cambridge University Press, 700 pp.

Webster, P. J., 1994: The role of hydrological processes in ocean-atmosphere interactions. *Rev. Geophys.,* **32** (4), 427–476.

Westwater, E. R., Y. Han, M. D. Shupe, and S. Y. Matrosov, 2001: Analysis of integrated cloud liquid and precipitable water vapor retrievals from microwave radiometers during the Surface Heat Budget of the Arctic Ocean project. *J. Geophys. Res.,* **106,** 32 019–32 030.

——, S. Crewell, and C. Mätzler, 2004: A review of surface-based microwave and millimeter-wave radiometric remote sensing of the troposphere. *Radio Sci. Bull.,* **310,** 59–80.

Whiteman, D. N., I. Veselovskii, M. Cadirola, K. Rush, J. Comer, J. R. Potter, and R. Tola, 2007: Demonstration measurements of water vapor, cirrus clouds, and carbon dioxide using a high-performance Raman lidar. *J. Atmos. Oceanic Technol.,* **24,** 1377–1388.

Yang, H., and R. T. Pierrehumbert, 1994: Production of dry air by isentropic mixing. *J. Atmos. Sci.,* **51,** 3437–3454.

Zhang, C., B. Mapes, and B. J. Soden, 2003: Bimodality in tropical water vapour. *Quart. J. Roy. Meteor. Soc.,* **129,** 2847–2866.